INTERNATIONAL JOURNAL FOR NUMERICAL METHODS IN ENGINEERING
Int. J. Numer. Meth. Engng 2004; **60**:2313–2333 (DOI: 10.1002/nme.1045)

Finite element formulation for modelling large deformations in elasto-viscoplastic polycrystals

Karel Matouš and Antoinette M. Maniatty*, †

Department of Mechanical, Aerospace, and Nuclear Engineering, Rensselaer Polytechnic Institute, Troy, NY 12180-3590, U.S.A.

SUMMARY

Anisotropic, elasto-viscoplastic behaviour in polycrystalline materials is modelled using a new, updated Lagrangian formulation based on a three-field form of the Hu-Washizu variational principle to create a stable finite element method in the context of nearly incompressible behaviour. The meso-scale is characterized by a representative volume element, which contains grains governed by single crystal behaviour. A new, fully implicit, two-level, backward Euler integration scheme together with an efficient finite element formulation, including consistent linearization, is presented. The proposed finite element model is capable of predicting non-homogeneous meso-fields, which, for example, may impact subsequent recrystallization. Finally, simple deformations involving an aluminium alloy are considered in order to demonstrate the algorithm. Copyright © 2004 John Wiley & Sons, Ltd.

KEY WORDS: polycrystal; finite element; integration algorithm; finite deformation; consistent tangent

1. INTRODUCTION

The mechanical properties of polycrystalline materials, such as yield and fatigue strength, anisotropy, etc., depend upon meso-structural features such as grain structure, both size and shape, and grain orientation distribution, among other things. The deformation and thermal histories during processing are key factors affecting these features, which evolve during processing due to deformation and recrystallization phenomena. In this work, the focus is on modelling the evolution of the grain structure and local crystallographic orientations during deformation. Thus, the modelling effort is centered at the meso-scale, i.e. the polycrystalline aggregate scale.

*Correspondence to: Maniatty, Department of Mechanical, Aerospace, and Nuclear Engineering, Rensselaer Polytechnic Institute, 110 8th Street, Troy, NY 12180-3590, U.S.A.
†E-mail: maniaa@rpi.edu

Contract/grant sponsor: National Science Foundation; contract/grant number: CMS–0084987, DMI–0115330, DMI–0115146
Contract/grant sponsor: Alcoa, Inc.

Received 31 March 2003
Revised 29 August 2003
Accepted 4 December 2003

Published online 4 June 2004

In modelling the behaviour of polycrystalline metals at the meso-scale, it is necessary to model both the individual grains (crystals) and their interactions. The behaviour of single crystal has been studied extensively over many years, for example: Taylor *et al*. [1] studied plastic deformation in single crystals; Hill and Rice [2] extended this study to rate-independent elastic–plastic deformations and Peirce *et al*. [3] described material rate dependence and localized deformation in crystalline solids, just to name a few. In order to model a polycrystal and link to the macro-scale, the interactions of the grains must be considered and an averaging procedure, or mean field hypothesis, is needed. One common approach is to assume homogeneous deformations and stresses within the individual grains, allowing incompatibility in the stress and/or displacement field across grain boundaries. In these cases, the macroscopic deformation and stress are taken to be the average over all the grains. For example, in the extended Taylor hypothesis [4, 5], each crystal is assumed to undergo the macroscopic deformation identically, and the overall stresses are computed by averaging local stresses in crystals. Other averaging approaches have also been proposed [6, 7]. Such models do not capture the non-homogeneous deformation fields within the grains, which are necessary to satisfy both compatibility and stress equilibrium across grain boundaries. It is these intra-grain heterogeneities that play an essential role in subsequent recrystallization phenomena and damage evolution. In order to model these heterogeneities, several researchers have modelled discretized, idealized grain structures in both two [8–10] and three dimensions [11]. More recently, Busso *et al*. [12] and Beaudoin *et al*. [13] have modelled three-dimensional, discretized, idealized grains together with gradient crystal plasticity models, albeit very different approaches considering different gradient fields, to capture grain size effects. Sarma *et al*. [14] consider a more realistic grain structure in three dimensions.

As mentioned above, several authors have presented finite element formulations for modelling discretized grains at the meso-scale. In many of these cases, a velocity-based formulation is used [11, 13–15], where the primary variable solved for in the finite element formulation is the velocity field, which is then multiplied by the incremental time step to update the geometry. Such formulations require small time steps both to preserve accuracy and to maintain convergence. Displacement-based finite element formulations, frequently implemented into the commercial finite element code ABAQUS, have also been described in the literature [9, 10, 12]. In these cases, the tangent matrix is typically formed using finite difference approximations.

The present work provides a new computational framework for modelling the mesoscopic behaviour of polycrystals at finite strains. The meso-scale is characterized by a representative volume element (RVE), commonly referred to as a unit cell, which contains an aggregate of grains. The polycrystal RVE is modelled with a displacement-based updated Lagrangian finite element formulation based on the Hu-Washizu variational principle. Because the behaviour of polycrystalline metal subjected to large strains is nearly incompressible, a mixed finite element method that interpolates the pressure and displacement fields separately is required. For Galerkin methods, the choice of interpolation functions must satisfy the Ladyzenskaya–Babuska–Brezzi condition (see e.g. Reference [16]) in order to achieve unique solvability, convergence, and robustness. Without balancing the interpolations properly, significant oscillations in the solution typically result. Numerous formulations that give stable solutions have been proposed [17–20], and in this work, a Hu-Washizu variation approach is applied. Consistent linearization is used to obtain an efficient algorithm, where large time steps can be taken. At the beginning of Section 2, we summarize the principal equations of the updated Lagrangian formulation including decomposition of the deformation gradient into elastic and plastic parts [21, 22].

A kinematic split of the deformation gradient into volume preserving and volumetric parts is used. A fully implicit two-level backward Euler integration scheme is presented in Section 3. In Section 4, we introduce the three-field form of the Hu-Washizu variational principle based on the kinematic split of the deformation gradient. Next, we describe the finite element formulation including the consistent linearization. Finally, examples are considered involving simple deformations in order to demonstrate the algorithm.

The symbolic notation adopted herein upper case boldface italic and lower case boldface Greek letters e.g. $\boldsymbol{P}$ and $\boldsymbol{\sigma}$ for second-order tensors. The trace of the second-order tensor is denoted as $\mathrm{tr}(\boldsymbol{A})$, and the tensor operations between two second-order tensors $\boldsymbol{S}$ and $\boldsymbol{E}$ are indicated as $\boldsymbol{SE}$ for a contraction of tensors (a second-order tensor) or $\boldsymbol{S} : \boldsymbol{E}$ for the scalar product (a double contraction). Furthermore, over-hat, e.g. $\hat{\boldsymbol{S}}$, denotes quantity $\boldsymbol{S}$ at the relaxed configuration, over-bar, e.g. $\bar{\boldsymbol{F}}$, denotes the volume preserving part of a tensor $\boldsymbol{F}$, and over-tilde, e.g. $\tilde{\boldsymbol{F}}$ denotes the finite element approximation of $\boldsymbol{F}$ computed from the finite element approximation of the displacement field.

2. CRYSTAL ELASTO-VISCOPLASTIC MODEL

First, let us assume the motion $\boldsymbol{\phi}(\boldsymbol{X}, t)$ and let $\boldsymbol{F}(\boldsymbol{X}, t) = \nabla\boldsymbol{\phi}(\boldsymbol{X}, t)$ be the deformation gradient at the current time $t \in \mathbb{R}^+$ with the Jacobian given by $J = \det(\boldsymbol{F})$. Here $\boldsymbol{X} \in \mathbb{R}^3$ designates the position of a particle in the reference configuration $B_0 \subset \mathbb{R}^3$ in the Cartesian co-ordinate system.

In general, the volume preserving part of a deformation, denoted with an over-bar ($\bar{}$), is

$$\bar{\boldsymbol{F}} = J^{-1/3}\boldsymbol{F} \tag{1}$$

and the volumetric part reads,

$$\theta = J \tag{2}$$

In this work, a kinematic split of the deformation gradient into volume preserving and volumetric parts is used to create a stable finite element method, avoiding oscillations in the solution for the pressure, in the context of nearly incompressible behaviour [17, 18]. Using an updated Lagrangian formulation and adopting the multiplicative decomposition of the deformation gradient into elastic and plastic parts [21, 22], we arrive at (Figure 1),

$$\begin{aligned}
\boldsymbol{F}_{n+1} &= \boldsymbol{F}_{\mathrm{r}}\boldsymbol{F}_n = \theta_{\mathrm{r}}^{1/3}\bar{\boldsymbol{F}}_{\mathrm{r}}\theta_n^{1/3}\bar{\boldsymbol{F}}_n \\
\boldsymbol{F}_{n+1} &= {}^{\mathrm{e}}\boldsymbol{F}_{n+1}{}^{\mathrm{p}}\boldsymbol{F}_{n+1} = \theta_{n+1}^{1/3}\,{}^{\mathrm{e}}\bar{\boldsymbol{F}}_{n+1}{}^{\mathrm{p}}\boldsymbol{F}_{n+1} \\
{}^{\mathrm{e}}\boldsymbol{F}_{n+1} &= \boldsymbol{F}_{\mathrm{r}}{}^{\mathrm{e}}\boldsymbol{F}_n{}^{\mathrm{p}}\boldsymbol{F}_{\mathrm{r}}^{-1} = \theta_{\mathrm{r}}^{1/3}\bar{\boldsymbol{F}}_{\mathrm{r}}{}^{\mathrm{e}}\boldsymbol{F}_n{}^{\mathrm{p}}\boldsymbol{F}_{\mathrm{r}}^{-1} \\
\boldsymbol{F}_* &= \boldsymbol{F}_{\mathrm{r}}{}^{\mathrm{e}}\boldsymbol{F}_n \\
{}^{\mathrm{p}}\boldsymbol{F}_{n+1} &= {}^{\mathrm{p}}\boldsymbol{F}_{\mathrm{r}}{}^{\mathrm{p}}\boldsymbol{F}_n
\end{aligned} \tag{3}$$

where right subscripts n and $n+1$ indicate times t_n and t_{n+1}, and left superscripts e and p denote elastic and plastic parts, respectively; $\boldsymbol{F}_{\mathrm{r}}$ is the relative deformation gradient and $\boldsymbol{F}_*$

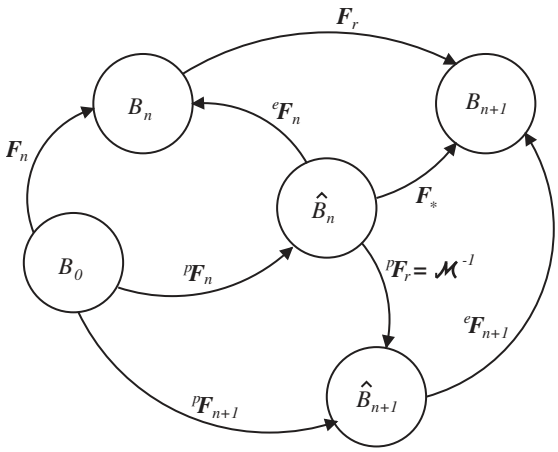

Figure 1. Kinematic decomposition of deformation gradients.

denotes the trial elastic deformation gradient. The plastic deformation gradient and the volume preserving part of the elastic deformation gradient satisfy,

$$\det({}^{\mathrm{p}}\boldsymbol{F}) = 1 \quad \text{and} \quad \det({}^{\mathrm{e}}\bar{\boldsymbol{F}}) = 1 \tag{4}$$

Symbol $\theta = \theta_{\mathrm{r}}\theta_n$ is now an additional variable entering the formulation and denotes a mixed representation for the determinant of the deformation gradient, $\theta \equiv \det(\boldsymbol{F})$. In the finite element formulation, Equation (2) is satisfied in a weak sense to provide stability. Then the relative deformation gradient is set as $\boldsymbol{F}_{\mathrm{r}} = \theta_{\mathrm{r}}^{1/3}\tilde{J}_{\mathrm{r}}^{-1/3}\tilde{\boldsymbol{F}}_{\mathrm{r}}$, $\tilde{J}_{\mathrm{r}} = \det(\tilde{\boldsymbol{F}}_{\mathrm{r}})$, where over-tilde ($\tilde{}$) denotes a quantity computed from the finite element approximation of the displacement field. Referring to Figure 1, the proposed formulation is based on moving relaxed configuration $\hat{B}_n \to \hat{B}_{n+1}$, which will lead to a specific finite element treatment.

We assume that crystallographic slip is the only mechanism for the plastic deformation. Such slip occurs due to dislocation motion through the crystal lattice, which can also undergo elastic stretch and rotation. Following the approach proposed by Maniatty *et al*. [23] and using the multiplicative decomposition of the deformation gradient, Equation (3_2), the velocity gradient yields

$$\boldsymbol{L} = {}^{\mathrm{e}}\dot{\boldsymbol{F}}\,{}^{\mathrm{e}}\boldsymbol{F}^{-1} + {}^{\mathrm{e}}\boldsymbol{F}\,{}^{\mathrm{p}}\hat{\boldsymbol{L}}\,{}^{\mathrm{e}}\boldsymbol{F}^{-1} \tag{5}$$

and

$${}^{\mathrm{p}}\hat{\boldsymbol{L}} = {}^{\mathrm{p}}\dot{\boldsymbol{F}}\,{}^{\mathrm{p}}\boldsymbol{F}^{-1} = \sum_{\alpha=1}^{N_{\mathrm{s}}} \dot{\gamma}^{\alpha}\boldsymbol{P}^{\alpha} \tag{6}$$

where ${}^{\mathrm{p}}\hat{\boldsymbol{L}}$ denotes the plastic velocity gradient on the relaxed configuration $\hat{B}$, as shown in Figure 1; $\dot{\gamma}^{\alpha}$ is the rate of shearing on the slip system α, and N_{s} denotes the number of slip systems for a crystal; $\boldsymbol{P}^{\alpha} = \boldsymbol{\mu}_1^{\alpha} \otimes \boldsymbol{\mu}_2^{\alpha}$ represents the Schmid tensor, where $\boldsymbol{\mu}_1^{\alpha}$, $\boldsymbol{\mu}_2^{\alpha}$ denote the α slip direction and slip plane normal, respectively. Note that the Schmid tensor $\boldsymbol{P}^{\alpha}$ is identical in both the reference B_0 and the relaxed $\hat{B}$ configurations.

In general, the Helmholtz free energy per unit volume stored in the system depends on the elastic behaviour, plastic state of deformation, and temperature. For the sake of simplicity, we neglect thermal effects and adopt the usual assumption that the elastic potential is unaffected by the plastic flow. In addition, it is assumed that the elastic behaviour is linear and elastic strains are small, typical for metals. Based on such observation, one can define the hyperelastic potential as,

$$\hat{W}({}^{\mathrm{e}}\boldsymbol{F}) = \tfrac{1}{2}\,{}^{\mathrm{e}}\hat{\boldsymbol{E}} : \mathscr{L} : {}^{\mathrm{e}}\hat{\boldsymbol{E}} \tag{7}$$

and the elastic constitutive stress strain relation on the relaxed configuration $\hat{B}$ reads,

$$\hat{\boldsymbol{S}} = 2\,\frac{\partial \hat{W}}{\partial\, {}^{\mathrm{e}}\boldsymbol{C}} = \mathscr{L} : {}^{\mathrm{e}}\hat{\boldsymbol{E}} \tag{8}$$

where ${}^{\mathrm{e}}\boldsymbol{C} = {}^{\mathrm{e}}\boldsymbol{F}^{\mathrm{T}}\,{}^{\mathrm{e}}\boldsymbol{F}$ denotes the right Cauchy–Green deformation tensor, ${}^{\mathrm{e}}\hat{\boldsymbol{E}} = \frac{1}{2}({}^{\mathrm{e}}\boldsymbol{C} - \mathbf{1})$ denotes the elastic Green–Lagrange strain tensor, $\mathscr{L}$ represents the fourth-order elasticity tensor and $\mathbf{1}$ is the second-order identity tensor; the second Piola–Kirchoff (P–K) stress $\hat{\boldsymbol{S}}$ can be expressed as the pull back of the Cauchy stress $\boldsymbol{\sigma}$ given by $\hat{\boldsymbol{S}} = \det({}^{\mathrm{e}}\boldsymbol{F})\,{}^{\mathrm{e}}\boldsymbol{F}^{-1}\boldsymbol{\sigma}\,{}^{\mathrm{e}}\boldsymbol{F}^{-\mathrm{T}}$.

The viscoplastic slip along crystallographic slip systems is modelled assuming a simple power law [23, 24],

$$\dot{\gamma}^{\alpha} = \dot{\gamma}_0 \frac{\tau^{\alpha}}{g^{\alpha}} \left| \frac{\tau^{\alpha}}{g^{\alpha}} \right|^{1/m-1} \tag{9}$$

where m is a material rate sensitivity parameter, $\dot{\gamma}_0$ is a reference rate and g^{α} denotes a resistance to plastic slip (hardness) on slip system α. The resolved shear stress τ^{α} is related to the second P–K stress as,

$$\tau^{\alpha} = ({}^{\mathrm{e}}\boldsymbol{C}\,\hat{\boldsymbol{S}}) : \boldsymbol{P}^{\alpha} \tag{10}$$

To describe the evolution of hardness on the slip systems, we adopt an approach proposed by Voce [25] and later modified by Kocks [26]. This approach assumes that effects of self and latent hardening are equivalent. Thus, all slip systems start with same hardness and harden together at the same rate. Therefore, the superscript α can be dropped from the hardness, and the evolution equation yields

$$\dot{g} = G(\dot{\gamma}, g)\dot{\gamma} = G_0 \left(\frac{g_{\mathrm{s}} - g}{g_{\mathrm{s}} - g_0} \right) \dot{\gamma} \tag{11}$$

where a hardening rate G_0 and an initial resolved shear strength g_0 are material parameters; $\dot{\gamma}$ denotes the total shearing rate on all slip systems

$$\dot{\gamma} = \sum_{\alpha=1}^{N_{\mathrm{s}}} |\dot{\gamma}^{\alpha}| \tag{12}$$

The saturation value of the hardness g_{s} is given by

$$g_{\mathrm{s}} = g_{\mathrm{s}_0} \left| \frac{\dot{\gamma}}{\dot{\gamma}_{\mathrm{s}}} \right|^{\omega} \tag{13}$$

where g_{s_0}, $\dot{\gamma}_s$ and ω are material parameters. There are numerous other models for slip system hardening, and the influence of assumptions about latent versus self hardening have been discussed in the literature, e.g. Reference [27]. In this work, the focus is on demonstrating the numerical algorithm. As a first step, the relatively simple, but widely used, hardening model described above is implemented. Implementing other models will not substantially change the algorithm, and future work will involve investigation of other slip system hardening models.

3. INTEGRATION PROCEDURE

For a prescribe deformation path, the stress response and hardness evolution can be obtained by integrating the constitutive equations presented in the previous Section. The proposed numerical procedure employs a fully implicit two-level backward Euler integration scheme together with a modified Lagrange variational principle to enforce the plastic incompressibility at the material scale. Here, it is assumed that the deformation is known from the overall finite element method, which will be described later in the article; in particular, all the primary quantities $\boldsymbol{F}_n$, $\hat{\boldsymbol{S}}_n$, τ_n and g_n are known at time t_n, and the finite element approximations of the relative deformation gradient $\tilde{\boldsymbol{F}}_r$ and of the relative volumetric deformation θ_r are given, where $t_{n+1} \equiv t_n + \Delta t$ and Δt is a time step.

In the first level of integration, applying a backward Euler scheme to integrate the plastic deformation gradient yields,

$$ {}^{p}\boldsymbol{F}_{n+1} = {}^{p}\boldsymbol{F}_n + \Delta t\, {}^{p}\dot{\boldsymbol{F}}_{n+1} = {}^{p}\boldsymbol{F}_n + \Delta t\, {}^{p}\hat{\boldsymbol{L}}_{n+1}\, {}^{p}\boldsymbol{F}_{n+1} \tag{14} $$

It should be noted that an exponential map may also be used to efficiently integrate Equation (6), see for example References [28, 29]. This results in the following when a backward Euler approach is maintained:

$$ \begin{aligned} {}^{p}\boldsymbol{F}_{n+1} &= \exp(\Delta t\, {}^{p}\hat{\boldsymbol{L}}_{n+1})\, {}^{p}\boldsymbol{F}_n = \left(\boldsymbol{I} + \Delta t\, {}^{p}\hat{\boldsymbol{L}}_{n+1} + \frac{\Delta t^2}{2}\, {}^{p}\hat{\boldsymbol{L}}_{n+1}\, {}^{p}\hat{\boldsymbol{L}}_{n+1} + \cdots \right) {}^{p}\boldsymbol{F}_n \\ &= {}^{p}\boldsymbol{F}_n + \Delta t\, {}^{p}\hat{\boldsymbol{L}}_{n+1}\, {}^{p}\boldsymbol{F}_n + \text{h.o.t.} \end{aligned} \tag{15} $$

In the present work, the plastic deformation step size in the integration is strongly restricted by the high degree of non-linearity of the constitutive model, typical for aluminium. As a result, the first higher order term in Equation (15) is four orders of magnitude smaller than the first order term, and, of course, Equation (14) is equivalent to Equation (15) to first order. Furthermore, since the result of the integration of ${}^{p}\boldsymbol{F}_{n+1}$ is restricted to the space where $\det({}^{p}\boldsymbol{F}_{n+1}) = 1$, the results from using either approach are not substantially different. In this work, the simple backward Euler form in Equation (14) is used.

After introducing Equation (6) into Equation (14) and keeping the hardness g fixed, in this first level, at its best available estimate, the inverse of the relative plastic deformation gradient is then,

$$ {}^{p}\boldsymbol{F}_r^{-1} = [\boldsymbol{1} - \Delta t\, {}^{p}\hat{\boldsymbol{L}}_{n+1}] \tag{16} $$

Furthermore, the plastic velocity gradient is given by

$$ {}^{\mathrm{p}}\hat{\boldsymbol{L}}_{n+1} = \sum_{\alpha=1}^{N_{\mathrm{s}}} \dot{\gamma}^{\alpha}_{n+1} \boldsymbol{P}^{\alpha} = \frac{1}{\Delta t}\left(\mathbf{1} - {}^{\mathrm{p}}\boldsymbol{F}_{\mathrm{r}}^{-1}\right) \tag{17} $$

Next, letting $\mathscr{M} \equiv {}^{\mathrm{p}}\boldsymbol{F}_{\mathrm{r}}^{-1}$, consider a modified Lagrange functional,

$$ \Pi_m(\mathscr{M}, \lambda) = \Pi(\mathscr{M}) + \lambda Ic(\mathscr{M}) \tag{18} $$

where

$$ \Pi(\mathscr{M}) = \frac{\Delta t}{2}\left[\sum_{\alpha=1}^{N_{\mathrm{s}}} \dot{\gamma}^{\alpha}_{n+1} \boldsymbol{P}^{\alpha} - \frac{1}{\Delta t}(\mathbf{1} - \mathscr{M})\right] : \left[\sum_{\alpha=1}^{N_{\mathrm{s}}} \dot{\gamma}^{\alpha}_{n+1} \boldsymbol{P}^{\alpha} - \frac{1}{\Delta t}(\mathbf{1} - \mathscr{M})\right] \tag{19} $$

λ represents the Lagrange multiplier, and the incompressibility constraint condition is,

$$ Ic(\mathscr{M}) = [\det(\mathscr{M}^{-1}{}^{\mathrm{p}}\boldsymbol{F}_n) - 1] = 0 \tag{20} $$

Solving the saddle point problem, $\inf \sup \Pi_m(\mathscr{M}, \lambda)$, we obtain a system of ten non-linear equations for the components of $\mathscr{M}$ and the Lagrange multiplier λ,

$$ \begin{aligned} \mathscr{R}_{\mathscr{M}} &= \frac{\partial \Pi_m}{\partial \mathscr{M}} = \sum_{\alpha=1}^{N_{\mathrm{s}}} \dot{\gamma}^{\alpha}_{n+1} \boldsymbol{P}^{\alpha} - \frac{1}{\Delta t}(\mathbf{1} - \mathscr{M}) - \lambda \det(\mathscr{M}^{-1}{}^{\mathrm{p}}\boldsymbol{F}_n)\mathscr{M}^{-\mathrm{T}} = \mathbf{0} \\ \mathscr{R}_{\lambda} &= \frac{\partial \Pi_m}{\partial \lambda} = [\det(\mathscr{M}^{-1}{}^{\mathrm{p}}\boldsymbol{F}_n) - 1] = 0 \end{aligned} \tag{21} $$

The Newton–Raphson iterative procedure is applied to solve this system and its linearization yields,

$$ \begin{bmatrix} \dfrac{\partial \mathscr{R}_{\mathscr{M}}}{\partial \mathscr{M}} & \dfrac{\partial \mathscr{R}_{\mathscr{M}}}{\partial \lambda} \\ \dfrac{\partial \mathscr{R}_{\lambda}}{\partial \mathscr{M}} & \dfrac{\partial \mathscr{R}_{\lambda}}{\partial \lambda} \end{bmatrix}^{k} \begin{Bmatrix} \Delta \mathscr{M} \\ \Delta \lambda \end{Bmatrix} = - \begin{Bmatrix} \mathscr{R}_{\mathscr{M}} \\ \mathscr{R}_{\lambda} \end{Bmatrix}^{k} \tag{22} $$

where for the $(k+1)$th iteration, the inverse of the relative plastic deformation gradient and the Lagrange multiplier are updated as $\mathscr{M}^{k+1} = \mathscr{M}^{k} + \Delta\mathscr{M}$ and $\lambda^{k+1} = \lambda^{k} + \Delta\lambda$, respectively. The linearized terms on the left-hand-side of Equation (22) are

$$ \begin{aligned} D\mathscr{R}_{\mathscr{M}}[\Delta\mathscr{M}] &= \sum_{\alpha=1}^{N_{\mathrm{s}}} \frac{\partial \dot{\gamma}^{\alpha}_{n+1}}{\partial \tau^{\alpha}_{n+1}} D\tau^{\alpha}_{n+1}[\Delta\mathscr{M}]\boldsymbol{P}^{\alpha} + \frac{1}{\Delta t}\Delta\mathscr{M} \\ &\quad + \lambda \det(\mathscr{M}^{-1}{}^{\mathrm{p}}\boldsymbol{F}_n)[\mathrm{tr}(\mathscr{M}^{-1}\Delta\mathscr{M})\mathscr{M}^{-\mathrm{T}} + (\mathscr{M}^{-1}\Delta\mathscr{M}\mathscr{M}^{-1})^{\mathrm{T}}] \\ D\mathscr{R}_{\mathscr{M}}[\Delta\lambda] &= -\det(\mathscr{M}^{-1}{}^{\mathrm{p}}\boldsymbol{F}_n)\mathscr{M}^{-\mathrm{T}}\Delta\lambda \\ D\mathscr{R}_{\lambda}[\Delta\mathscr{M}] &= -\det(\mathscr{M}^{-1}{}^{\mathrm{p}}\boldsymbol{F}_n)\mathscr{M}^{-\mathrm{T}} : \Delta\mathscr{M} \\ D\mathscr{R}_{\lambda}[\Delta\lambda] &= 0 \end{aligned} \tag{23} $$

where

$$\frac{\partial \dot{\gamma}^{\alpha}_{n+1}}{\partial \tau^{\alpha}_{n+1}} = \frac{\dot{\gamma}_0}{m g_{n+1}} \left| \frac{\tau^{\alpha}_{n+1}}{g_{n+1}} \right|^{1/m-1} \tag{24}$$

The notation $\mathscr{R}^{k+1}_{\boldsymbol{y}} \approx \mathscr{R}^{k}_{\boldsymbol{y}} + D\mathscr{R}_{\boldsymbol{y}}[\Delta \boldsymbol{y}] = \boldsymbol{0}$ is employed in this paper for consistent linearization of a non-linear system $\mathscr{R}_{\boldsymbol{y}} = \boldsymbol{0}$, where a solution $\boldsymbol{y}^{k+1} = \boldsymbol{y}^{k} + \Delta \boldsymbol{y}$ at iteration $k+1$ is obtained using Newton's iterative method. The consistent linearization of the resolved shear stress τ^{α}_{n+1} can be obtained using Equations (3), (8) and (10),

$$D\tau^{\alpha}_{n+1}[\Delta \mathscr{M}] = \{\boldsymbol{F}^{\mathrm{T}\mathrm{e}}_{*} \boldsymbol{F}_{n+1} \mathscr{G}^{\alpha}\} : \Delta \mathscr{M} \tag{25}$$

where

$$\mathscr{G}^{\alpha} = \hat{\boldsymbol{S}}_{n+1} \boldsymbol{P}^{\alpha \mathrm{T}} + \boldsymbol{P}^{\alpha} \hat{\boldsymbol{S}}_{n+1} + \mathscr{L} : ({}^{\mathrm{e}}\boldsymbol{C}_{n+1} \boldsymbol{P}^{\alpha}) \tag{26}$$

and $\boldsymbol{F}_{*} = \boldsymbol{F}_{\mathrm{r}}{}^{\mathrm{e}}\boldsymbol{F}_{n} = \theta_{\mathrm{r}}^{1/3} \tilde{J}_{\mathrm{r}}^{-1/3} \tilde{\boldsymbol{F}}_{\mathrm{r}}{}^{\mathrm{e}}\boldsymbol{F}_{n}$, as shown in Figure 1. It is noted that the quantities at time t_{n+1} in Equations (24) and (26) are evaluated at the kth iteration.

Once a solution for $\mathscr{M}$ and λ is known, the second level of the algorithm provides a solution for the hardness. Integrating Equation (11) with a backward Euler scheme, and keeping $\mathscr{M}$, τ^{α}_{n+1} and $\dot{\gamma}^{\alpha}_{n+1}$ fixed, one obtains,

$$g_{n+1} = \frac{(g_{\mathrm{s}n+1} - g_0) g_n + \Delta t G_0 g_{\mathrm{s}n+1} \dot{\gamma}_{n+1}}{(g_{\mathrm{s}n+1} - g_0) + \Delta t G_0 \dot{\gamma}_{n+1}} \tag{27}$$

where $\dot{\gamma}_{n+1}$ and $g_{\mathrm{s}n+1}$ are given by Equations (12) and (13). Now the new hardness g_{n+1} is used in the first level of the integration scheme, Equations (21)–(25), and the staggered procedure is repeated until global convergence is obtained. Usually, less that ten iterations k are sufficient in the first level of procedure to reach the convergence criterion on residuals,

$$\|\mathscr{R}_{\mathscr{M}}\| + \|\mathscr{R}_{\lambda}\| \leqslant \mathrm{tol} = 10^{-5} \tag{28}$$

and only three to five global iterations are necessary to achieve a tolerance for,

$$\frac{\|g^{k+1}_{n+1} - g^{k}_{n+1}\|}{\|g_0\|} \leqslant \mathrm{tol} = 10^{-5} \tag{29}$$

For quick convergence, it is important to take a good initial guess of $\mathscr{M}$. Since the elastic deformations are generally small, it is assumed that the total increment of deformation is plastic for the initial guess, i.e.

$${}^{\mathrm{p}}\boldsymbol{F}^{k=0}_{n+1} = {}^{\mathrm{e}}\boldsymbol{F}^{-1}_{n} \boldsymbol{F}_{n+1} \Rightarrow \mathscr{M}^{k=0} = {}^{\mathrm{e}}\boldsymbol{F}^{-1}_{n} \boldsymbol{F}^{-1}_{\mathrm{r}} {}^{\mathrm{e}}\boldsymbol{F}_{n} \tag{30}$$

Moreover, if the solution for $\mathscr{M}$ and g is not found within a user specified number of iterations, a command is passed to the global finite element environment to change time and load steps, as will be described later.

4. FINITE ELEMENT FORMULATION

In this section, the variational formulation and numerical treatment of the elasto-viscoplastic boundary value problem by the finite element method are outlined. The present finite element formulation is based on a kinematic split of the deformation gradient into volume-preserving (deviatoric) and volumetric parts together with a three-field form of the Hu-Washizu variational principle [17–19] to treat volume constraints arising from the nearly incompressible behaviour due to the isochoric plastic flow.

Let $\boldsymbol{x} = \boldsymbol{\phi}(\boldsymbol{X}, t)$ be the spatial co-ordinates of a particle and $\boldsymbol{x}_{n+1} = \boldsymbol{X} + \boldsymbol{u}_{n+1}$, where $\boldsymbol{u}_{n+1} = \boldsymbol{u}_n + \boldsymbol{u}$ denotes the incremental displacement field. Further, let $\tilde{\boldsymbol{F}}_{\mathrm{r}} = [\boldsymbol{1} + \nabla \boldsymbol{u}]$ represents the relative deformation gradient, where ∇ is a gradient with respect to $\boldsymbol{x}_n$. Next, consider the Lagrangian functional written as,

$$\Pi_L(\boldsymbol{u}, \theta_{\mathrm{r}}, p) = \frac{1}{2} \int_{B_n} \frac{1}{\det(\tilde{\boldsymbol{F}}_n)} {}^{\mathrm{e}}\hat{\boldsymbol{E}} : \mathscr{L} : {}^{\mathrm{e}}\hat{\boldsymbol{E}} \, \mathrm{d}V_n + \int_{B_n} \frac{1}{\det(\tilde{\boldsymbol{F}}_n)} p(\tilde{J}_{\mathrm{r}} \tilde{J}_n - \theta_{\mathrm{r}} \theta_n) \, \mathrm{d}V_n + L_{\mathrm{ext}} \tag{31}$$

with

$${}^{\mathrm{e}}\hat{\boldsymbol{E}} = \tfrac{1}{2} \left(\theta_{\mathrm{r}}^{2/3} \tilde{J}_{\mathrm{r}}^{-2/3} \mathscr{M}^{\mathrm{T}} {}^{\mathrm{e}}\boldsymbol{F}_n^{\mathrm{T}} \tilde{\boldsymbol{F}}_{\mathrm{r}}^{\mathrm{T}} \tilde{\boldsymbol{F}}_{\mathrm{r}} {}^{\mathrm{e}}\boldsymbol{F}_n \mathscr{M} - \boldsymbol{1} \right) \tag{32}$$

where $p = (\frac{1}{3})(\mathrm{tr}\, \boldsymbol{\sigma})$ is the hydrostatic stress; L_{ext} denotes a total potential energy associated with body forces $\boldsymbol{f}(\boldsymbol{x})$ and prescribed tractions $\breve{\boldsymbol{t}}(\boldsymbol{x})$ on the boundary $\boldsymbol{\phi}(\partial B_{\boldsymbol{\sigma}})$.

The condition of stationarity for the functional $\Pi_L(\boldsymbol{u}, \theta_{\mathrm{r}}, p)$ is given by

$$\inf_{\boldsymbol{u} \in U} \inf_{\theta_{\mathrm{r}} \in Q} \sup_{p \in Q} \Pi_L(\boldsymbol{u}, \theta_{\mathrm{r}}, p) \tag{33}$$

and

$$\begin{aligned} &U \subset [H^1]^N, \quad \boldsymbol{u} = \breve{\boldsymbol{u}} \text{ on } \boldsymbol{\phi}(\partial B_{\boldsymbol{u}}) \\ &Q \subset L_2 \end{aligned} \tag{34}$$

where N being the space dimension, H^1 represents the Sobolev space, and $\boldsymbol{\phi}(\partial B_{\boldsymbol{u}})$ is the boundary on which displacements $\breve{\boldsymbol{u}}$ are prescribed. Following standard variational methods, the resulting system of non-linear equations yields,

$$\begin{aligned} \mathscr{R}_{\boldsymbol{u}} \equiv \frac{\partial \Pi_L}{\partial \boldsymbol{u}} \delta \boldsymbol{u} &= \int_{B_n} \frac{1}{\det(\tilde{\boldsymbol{F}}_n)} \{ \theta_{\mathrm{r}}^{2/3} \tilde{J}_{\mathrm{r}}^{-2/3} \mathscr{A}(\delta \boldsymbol{u}) : \hat{\boldsymbol{S}} + p \tilde{J}_{\mathrm{r}} \tilde{J}_n \mathrm{tr}(\tilde{\boldsymbol{F}}_{\mathrm{r}}^{-1} \nabla \delta \boldsymbol{u}) \} \, \mathrm{d}V_n \\ &\quad - \int_{\partial B_\sigma} \frac{1}{\det(\tilde{\boldsymbol{F}}_n)} \breve{\boldsymbol{t}} \cdot \delta \boldsymbol{u} \, \mathrm{d}A_n - \int_{B_n} \frac{1}{\det(\tilde{\boldsymbol{F}}_n)} \boldsymbol{f} \cdot \delta \boldsymbol{u} \, \mathrm{d}V_n \\ \mathscr{R}_p \equiv \frac{\partial \Pi_L}{\partial p} \delta p &= \int_{B_n} \frac{1}{\det(\tilde{\boldsymbol{F}}_n)} \{ \tilde{J}_{\mathrm{r}} \tilde{J}_n - \theta_{\mathrm{r}} \theta_n \} \delta p \, \mathrm{d}V_n \\ \mathscr{R}_\theta \equiv \frac{\partial \Pi_L}{\partial \theta_{\mathrm{r}}} \delta \theta_{\mathrm{r}} &= \int_{B_n} \frac{1}{\det(\tilde{\boldsymbol{F}}_n)} \left\{ \tfrac{1}{3} \theta_{\mathrm{r}}^{-1/3} \tilde{J}_{\mathrm{r}}^{-2/3} \mathscr{B} : \hat{\boldsymbol{S}} - p \theta_n \right\} \delta \theta_{\mathrm{r}} \, \mathrm{d}V_n \end{aligned} \tag{35}$$

where $\delta \boldsymbol{u}, \delta p, \delta\theta_{\mathrm{r}}$ are arbitrary functions satisfying,

$$\begin{gathered} \delta \boldsymbol{u} \in U, \quad \delta \boldsymbol{u} = \boldsymbol{0} \text{ on } \boldsymbol{\phi}(\partial B_{\boldsymbol{u}}) \\ \delta p, \delta\theta_{\mathrm{r}} \in Q \end{gathered} \tag{36}$$

and

$$\begin{gathered} \mathscr{A}(\delta \boldsymbol{u}) = \mathscr{M}^{\mathrm{T}} \mathscr{C}(\delta \boldsymbol{u}) \mathscr{M}, \quad \mathscr{C}(\delta \boldsymbol{u}) = {}^{\mathrm{e}}\boldsymbol{F}_n^{\mathrm{T}} [(\nabla \delta \boldsymbol{u}^{\mathrm{T}} \tilde{\boldsymbol{F}}_{\mathrm{r}})^{\mathrm{sym}} - \tfrac{1}{3} \tilde{\boldsymbol{F}}_{\mathrm{r}}^{\mathrm{T}} \tilde{\boldsymbol{F}}_{\mathrm{r}} \operatorname{tr}(\tilde{\boldsymbol{F}}_{\mathrm{r}}^{-1} \nabla \delta \boldsymbol{u})] {}^{\mathrm{e}}\boldsymbol{F}_n \\ \mathscr{B} = \mathscr{M}^{\mathrm{T}} \mathscr{D} \mathscr{M}, \quad \mathscr{D} = {}^{\mathrm{e}}\boldsymbol{F}_n^{\mathrm{T}} \tilde{\boldsymbol{F}}_{\mathrm{r}}^{\mathrm{T}} \tilde{\boldsymbol{F}}_{\mathrm{r}} {}^{\mathrm{e}}\boldsymbol{F}_n \end{gathered} \tag{37}$$

4.1. Linearization

The finite element method together with a standard Newton–Raphson method is applied to solve the non-linear system equations (35). While an accurate integration of the constitutive equations is necessary to update stresses and the internal state variables, the formation of a tangent stiffness tensor that is consistent with the integration procedure is essential to maintain a quadratic rate of convergence [30], if one is to employ the standard Newton–Raphson method in solving the above system. A consistent linearization for the set of non-linear equations given in Equations (35), about a configuration $\boldsymbol{u}, \theta_{\mathrm{r}}, p$, is given by

$$\begin{aligned} D\mathscr{R}_{\boldsymbol{u}}[\Delta \boldsymbol{u}] + D\mathscr{R}_{\boldsymbol{u}}[\Delta p] + D\mathscr{R}_{\boldsymbol{u}}[\Delta\theta_{\mathrm{r}}] &= -\mathscr{R}_{\boldsymbol{u}} \\ D\mathscr{R}_{p}[\Delta \boldsymbol{u}] + 0 - D\mathscr{R}_{p}[\Delta\theta_{\mathrm{r}}] &= -\mathscr{R}_{p} \\ D\mathscr{R}_{\theta}[\Delta \boldsymbol{u}] - D\mathscr{R}_{\theta}[\Delta p] + D\mathscr{R}_{\theta}[\Delta\theta_{\mathrm{r}}] &= -\mathscr{R}_{\theta} \end{aligned} \tag{38}$$

where

$$\begin{aligned} D\mathscr{R}_{\boldsymbol{u}}[\Delta \boldsymbol{u}] = \int_{B_n} \frac{1}{\det(\tilde{\boldsymbol{F}}_n)} \Bigg\{ & \underbrace{\theta_{\mathrm{r}}^{4/3} \tilde{J}_{\mathrm{r}}^{-4/3} \mathscr{A}(\delta \boldsymbol{u}) : \mathscr{L} : \mathscr{A}(\Delta \boldsymbol{u})}_{\text{elastic material contribution}} + \underbrace{\theta_{\mathrm{r}}^{2/3} \tilde{J}_{\mathrm{r}}^{-2/3} \mathscr{M}^{\mathrm{T}} {}^{\mathrm{e}}\boldsymbol{F}_n^{\mathrm{T}} \mathscr{E} {}^{\mathrm{e}}\boldsymbol{F}_n \mathscr{M} : \hat{\boldsymbol{S}}}_{\text{elastic geometric contribution}} \\ & + \underbrace{\theta_{\mathrm{r}}^{4/3} \tilde{J}_{\mathrm{r}}^{-4/3} \mathscr{A}(\delta \boldsymbol{u}) : \mathscr{L} : [(D\mathscr{M}[\Delta \boldsymbol{u}])^{\mathrm{T}} \mathscr{D} \mathscr{M}]^{\mathrm{sym}}}_{\text{plastic material contribution}} \\ & + \underbrace{2\theta_{\mathrm{r}}^{2/3} \tilde{J}_{\mathrm{r}}^{-2/3} [(D\mathscr{M}[\Delta \boldsymbol{u}])^{\mathrm{T}} \mathscr{C} \mathscr{M}]^{\mathrm{sym}} : \hat{\boldsymbol{S}}}_{\text{plastic geometric contribution}} \\ & + \underbrace{p \tilde{J}_{\mathrm{r}} \tilde{J}_n [\operatorname{tr}(\tilde{\boldsymbol{F}}_{\mathrm{r}}^{-1} \nabla(\Delta \boldsymbol{u})) \operatorname{tr}(\tilde{\boldsymbol{F}}_{\mathrm{r}}^{-1} \nabla \delta \boldsymbol{u}) - \operatorname{tr}(\tilde{\boldsymbol{F}}_{\mathrm{r}}^{-1} \nabla(\Delta \boldsymbol{u}) \tilde{\boldsymbol{F}}_{\mathrm{r}}^{-1} \delta \boldsymbol{u})]}_{\text{pressure geometric contribution}} \Bigg\} \, \mathrm{d}V_n \end{aligned}$$

$$
\begin{aligned}
D\mathscr{R}_{\boldsymbol{u}}[\Delta\theta_{\mathrm{r}}] = \int_{B_n} \frac{1}{\det(\tilde{\boldsymbol{F}}_n)} \Big\{ & \tfrac{2}{3}\theta_{\mathrm{r}}^{-1/3}\tilde{J}_{\mathrm{r}}^{-2/3}\mathscr{A}(\delta\boldsymbol{u}) : \hat{\boldsymbol{S}}\Delta\theta_{\mathrm{r}} \\
& + 2\theta_{\mathrm{r}}^{2/3}\tilde{J}_{\mathrm{r}}^{-2/3}[(D\mathscr{M}[\Delta\theta_{\mathrm{r}}])^{\mathrm{T}}\mathscr{C}\mathscr{M}]^{\mathrm{sym}} : \hat{\boldsymbol{S}} \\
& + \tfrac{1}{3}\theta_{\mathrm{r}}^{1/3}\tilde{J}_{\mathrm{r}}^{-4/3}\mathscr{A}(\delta\boldsymbol{u}) : \mathscr{L} : \mathscr{B}\Delta\theta_{\mathrm{r}} \\
& + \theta_{\mathrm{r}}^{4/3}\tilde{J}_{\mathrm{r}}^{-4/3}\mathscr{A}(\delta\boldsymbol{u}) : \mathscr{L} : [(D\mathscr{M}[\Delta\theta_{\mathrm{r}}])^{\mathrm{T}}\mathscr{D}\mathscr{M}]^{\mathrm{sym}} \Big\}\, \mathrm{d}V_n \\
D\mathscr{R}_{\theta}[\Delta\boldsymbol{u}] = \int_{B_n} \frac{1}{\det(\tilde{\boldsymbol{F}}_n)} \Big\{ & \tfrac{2}{3}\theta_{\mathrm{r}}^{-1/3}\tilde{J}_{\mathrm{r}}^{-2/3}\mathscr{A}(\Delta\boldsymbol{u}) : \hat{\boldsymbol{S}} \\
& + \tfrac{2}{3}\theta_{\mathrm{r}}^{-1/3}\tilde{J}_{\mathrm{r}}^{-2/3}[(D\mathscr{M}[\Delta\boldsymbol{u}])^{\mathrm{T}}\mathscr{D}\mathscr{M}]^{\mathrm{sym}} : \hat{\boldsymbol{S}} \\
& + \tfrac{1}{3}\theta_{\mathrm{r}}^{1/3}\tilde{J}_{\mathrm{r}}^{-4/3}\mathscr{B} : \mathscr{L} : \mathscr{A}(\Delta\boldsymbol{u}) \\
& + \tfrac{1}{3}\theta_{\mathrm{r}}^{1/3}\tilde{J}_{\mathrm{r}}^{-4/3}[(D\mathscr{M}[\Delta\boldsymbol{u}])^{\mathrm{T}}\mathscr{D}\mathscr{M}]^{\mathrm{sym}} : \mathscr{L} : \mathscr{B} \Big\}\, \mathrm{d}V_n \\
D\mathscr{R}_{\theta}[\Delta\theta_{\mathrm{r}}] = \int_{B_n} \frac{1}{\det(\tilde{\boldsymbol{F}}_n)} \Big\{ & -\tfrac{1}{9}\theta_{\mathrm{r}}^{-4/3}\tilde{J}_{\mathrm{r}}^{-2/3}\mathscr{B} : \hat{\boldsymbol{S}}\Delta\theta_{\mathrm{r}} \\
& + \tfrac{2}{3}\theta_{\mathrm{r}}^{-1/3}\tilde{J}_{\mathrm{r}}^{-2/3}[(D\mathscr{M}[\Delta\theta_{\mathrm{r}}])^{\mathrm{T}}\mathscr{D}\mathscr{M}]^{\mathrm{sym}} : \hat{\boldsymbol{S}} \\
& + \tfrac{1}{9}\theta_{\mathrm{r}}^{-2/3}\tilde{J}_{\mathrm{r}}^{-4/3}\mathscr{B} : \mathscr{L} : \mathscr{B}\Delta\theta_{\mathrm{r}} \\
& + \tfrac{1}{3}\theta_{\mathrm{r}}^{1/3}\tilde{J}_{\mathrm{r}}^{-4/3}\mathscr{B} : \mathscr{L} : [(D\mathscr{M}[\Delta\theta_{\mathrm{r}}])^{\mathrm{T}}\mathscr{D}\mathscr{M}]^{\mathrm{sym}} \Big\}\, \mathrm{d}V_n \\
D\mathscr{R}_p[\Delta\theta_{\mathrm{r}}] \equiv D\mathscr{R}_{\theta}[\Delta p] = & \int_{B_n} \frac{1}{\det(\tilde{\boldsymbol{F}}_n)}\{\theta_n\delta\theta_{\mathrm{r}}\}\, \mathrm{d}V_n\Delta p \\
D\mathscr{R}_p[\Delta\boldsymbol{u}] \equiv D\mathscr{R}_{\boldsymbol{u}}[\Delta p] = & \int_{B_n} \tilde{J}_{\mathrm{r}}\mathrm{tr}(\tilde{\boldsymbol{F}}_{\mathrm{r}}^{-1}\nabla\delta\boldsymbol{u})\, \mathrm{d}V_n\Delta p
\end{aligned}
\tag{39}
$$

and

$$
\begin{aligned}
\mathscr{E} = {} & [\nabla\delta\boldsymbol{u}^{\mathrm{T}}\nabla(\Delta\boldsymbol{u})]^{\mathrm{sym}} + \tfrac{1}{3}\tilde{\boldsymbol{F}}_{\mathrm{r}}^{\mathrm{T}}\tilde{\boldsymbol{F}}_{\mathrm{r}}[\mathrm{tr}(\nabla(\Delta\boldsymbol{u})\tilde{\boldsymbol{F}}_{\mathrm{r}}^{-1}\nabla\delta\boldsymbol{u}\tilde{\boldsymbol{F}}_{\mathrm{r}}^{-1}) + \tfrac{2}{3}\,\mathrm{tr}(\tilde{\boldsymbol{F}}_{\mathrm{r}}^{-1}\nabla(\Delta\boldsymbol{u}))\mathrm{tr}(\tilde{\boldsymbol{F}}_{\mathrm{r}}^{-1}\nabla\delta\boldsymbol{u})] \\
& - \tfrac{2}{3}\,\mathrm{tr}(\tilde{\boldsymbol{F}}_{\mathrm{r}}^{-1}\nabla(\Delta\boldsymbol{u}))(\tilde{\boldsymbol{F}}_{\mathrm{r}}^{\mathrm{T}}\nabla\delta\boldsymbol{u})^{\mathrm{sym}} - \tfrac{2}{3}\,\mathrm{tr}(\tilde{\boldsymbol{F}}_{\mathrm{r}}^{-1}\nabla\delta\boldsymbol{u})(\tilde{\boldsymbol{F}}_{\mathrm{r}}^{\mathrm{T}}\nabla(\Delta\boldsymbol{u}))^{\mathrm{sym}}
\end{aligned}
\tag{40}
$$

The resulting tangent stiffness tensor is non-symmetric in the present analysis. Several finite element approximation schemes can be used within the proposed variational framework provided by Equation (31). In this work, discontinuous pressure and Jacobian interpolations are assumed, which enables these fields to be eliminated at the element level leading to a generalized displacement method, as in References [17, 18, 31]. The system of linear equations, Equation (38), is solved using sparse direct solver UMFPACK [32–34]. It still remains to

determine linearization of the relative plastic deformation gradient, $D\mathscr{M}[\Delta\boldsymbol{u}]$ and $D\mathscr{M}[\Delta\theta_{\mathrm{r}}]$, respectively. This will be described in the following subsection.

4.2. Linearization of $\mathscr{M}$ with respect to $\boldsymbol{u}$ and θ_{r}

First let us recall that the inverse of the relative plastic deformation gradient and the hardness are given in our integration algorithm as Equations (9), (11), (16), (27),

$$
\begin{aligned}
{}^{\mathrm{p}}\boldsymbol{F}_{\mathrm{r}}^{-1} \equiv \mathscr{M} &= \left[\mathbf{1} - \Delta t \sum_{\alpha=1}^{N_{\mathrm{s}}} \dot{\gamma}^{\alpha} \boldsymbol{P}^{\alpha}\right], \quad \dot{\gamma}^{\alpha} = \dot{\gamma}_{n+1}(\tau_{n+1}^{\alpha}, g_{n+1}) \\
g_{n+1} &= \frac{(g_{\mathrm{s}n+1} - g_0) g_n + \Delta t G_0 g_{\mathrm{s}n+1} \dot{\gamma}_{n+1}}{(g_{\mathrm{s}n+1} - g_0) + \Delta t G_0 \dot{\gamma}_{n+1}}, \quad \dot{g} = G(\dot{\gamma}_{n+1}, g_{n+1}) \dot{\gamma}_{n+1}
\end{aligned}
\tag{41}
$$

Using the implicit integration scheme for the plastic deformation gradient, Equation (14), and the hardness, Equation (27), linearization $D\mathscr{M}[\Delta\boldsymbol{u}]$ and $Dg_{n+1}[\Delta\boldsymbol{u}]$ yield,

$$
\begin{aligned}
D\mathscr{M}[\Delta\boldsymbol{u}] &= -\Delta t \sum_{\alpha=1}^{N_{\mathrm{s}}} \left(\frac{\partial \dot{\gamma}_{n+1}^{\alpha}}{\partial \tau_{n+1}^{\alpha}} D\tau_{n+1}^{\alpha}[\Delta\boldsymbol{u}] + \frac{\partial \dot{\gamma}_{n+1}^{\alpha}}{\partial g_{n+1}} Dg_{n+1}[\Delta\boldsymbol{u}] \right) \boldsymbol{P}^{\alpha} \\
Dg_{n+1}[\Delta\boldsymbol{u}] &= \mathfrak{K}_1 \sum_{\alpha=1}^{N_{\mathrm{s}}} \mathfrak{K}_2^{\alpha} D\tau_{n+1}^{\alpha}[\Delta\boldsymbol{u}]
\end{aligned}
\tag{42}
$$

where

$$
\begin{aligned}
\mathfrak{K}_1 &= \frac{\mathfrak{K}_4}{1 - \mathfrak{K}_4 \sum_{\alpha=1}^{N_{\mathrm{s}}} \dot{\gamma}_{n+1}^{\alpha} / |\dot{\gamma}_{n+1}^{\alpha}| \, \partial \dot{\gamma}_{n+1}^{\alpha} / \partial g_{n+1}}, \quad \mathfrak{K}_2^{\alpha} = \frac{\dot{\gamma}_{n+1}^{\alpha}}{|\dot{\gamma}_{n+1}^{\alpha}|} \frac{\partial \dot{\gamma}_{n+1}^{\alpha}}{\partial \tau_{n+1}^{\alpha}}, \quad \mathfrak{K}_3 = \frac{g_{\mathrm{s}0}\omega}{\dot{\gamma}_{\mathrm{s}}} \left| \frac{\dot{\gamma}_{n+1}}{\dot{\gamma}_{\mathrm{s}}} \right|^{\omega-1} \\
\mathfrak{K}_4 &= \Delta t G_0 \frac{\mathfrak{K}_3 \dot{\gamma}_{n+1} (g_n - g_0 + \Delta t G_0 \dot{\gamma}_{n+1}) + g_{\mathrm{s}_{n+1}} (g_{\mathrm{s}_{n+1}} - g_0 - g_n) + g_0 g_n}{(g_{\mathrm{s}_{n+1}} - g_0 - g_n + \Delta t G_0 \dot{\gamma}_{n+1})^2}
\end{aligned}
\tag{43}
$$

and

$$
\frac{\partial \dot{\gamma}_{n+1}^{\alpha}}{\partial \tau_{n+1}^{\alpha}} = \frac{\dot{\gamma}_0}{m g_{n+1}} \left| \frac{\tau_{n+1}^{\alpha}}{g_{n+1}} \right|^{1/m-1}, \quad \frac{\partial \dot{\gamma}_{n+1}^{\alpha}}{\partial g_{n+1}} = -\frac{\dot{\gamma}_0 \tau_{n+1}^{\alpha}}{m g_{n+1}^2} \left| \frac{\tau_{n+1}^{\alpha}}{g_{n+1}} \right|^{1/m-1} \tag{44}
$$

After substituting Equation (42_2) into Equation (42_1) and computing linearized term $D\tau_{n+1}^{\alpha}[\Delta\boldsymbol{u}]$, we obtain a tensor equation in the form,

$$
D\mathscr{M}[\Delta\boldsymbol{u}] : \mathfrak{A} = -\nabla(\Delta\boldsymbol{u}) : \mathfrak{B} \tag{45}
$$

where

$$
\begin{aligned}
\mathfrak{A} &= \frac{1}{\Delta t} \boldsymbol{I} + \sum_{\alpha=1}^{N_{\mathrm{s}}} \frac{\partial \dot{\gamma}_{n+1}^{\alpha}}{\partial \tau_{n+1}^{\alpha}} (\mathfrak{C}^{\alpha} \otimes \boldsymbol{P}^{\alpha}) + \mathfrak{K}_1 \left(\sum_{\alpha=1}^{N_{\mathrm{s}}} \mathfrak{K}_2^{\alpha} \mathfrak{C}^{\alpha} \right) \otimes \left(\sum_{\beta=1}^{N_{\mathrm{s}}} \frac{\partial \dot{\gamma}_{n+1}^{\beta}}{\partial g_{n+1}} \boldsymbol{P}^{\beta} \right) \\
\mathfrak{B} &= \sum_{\alpha=1}^{N_{\mathrm{s}}} \frac{\partial \dot{\gamma}_{n+1}^{\alpha}}{\partial \tau_{n+1}^{\alpha}} (\mathfrak{D}^{\alpha} \otimes \boldsymbol{P}^{\alpha}) + \mathfrak{K}_1 \left(\sum_{\alpha=1}^{N_{\mathrm{s}}} \mathfrak{K}_2^{\alpha} \mathfrak{D}^{\alpha} \right) \otimes \left(\sum_{\beta=1}^{N_{\mathrm{s}}} \frac{\partial \dot{\gamma}_{n+1}^{\beta}}{\partial g_{n+1}} \boldsymbol{P}^{\beta} \right)
\end{aligned}
\tag{46}
$$

and

$$\begin{aligned}\mathfrak{C}^{\alpha} &= \mathscr{M}^{-\mathrm{T}^{\mathrm{e}}}\boldsymbol{C}_{n+1}\mathscr{G}^{\alpha}\\ \mathfrak{D}^{\alpha} &= \theta_{\mathrm{r}}^{1/3}\tilde{J}_{\mathrm{r}}^{-1/3^{\mathrm{e}}}\boldsymbol{F}_{n+1}\mathscr{G}^{\alpha}\mathscr{M}^{\mathrm{T}^{\mathrm{e}}}\boldsymbol{F}_{n}^{\mathrm{T}} - \tfrac{1}{3}({}^{\mathrm{e}}\boldsymbol{C}_{n+1} : \mathscr{G}^{\alpha})\tilde{\boldsymbol{F}}_{\mathrm{r}}^{-\mathrm{T}}\end{aligned} \tag{47}$$

Note that $\boldsymbol{I}$ is the fourth order identity tensor, $\otimes$ denotes dyadic product, and $\mathscr{G}^{\alpha}$ is given by Equation (26). Inverting the fourth order tensor on the left-hand side of Equation (45) allows for the linearized form $D\mathscr{M}[\Delta\boldsymbol{u}]$ to be determined.

Likewise,

$$\begin{aligned}D\mathscr{M}[\Delta\theta_{\mathrm{r}}] &= -\Delta t\sum_{\alpha=1}^{N_{\mathrm{s}}}\left(\frac{\partial\dot{\gamma}_{n+1}^{\alpha}}{\partial\tau_{n+1}^{\alpha}}\,D\tau_{n+1}^{\alpha}[\Delta\theta_{\mathrm{r}}] + \frac{\partial\dot{\gamma}_{n+1}^{\alpha}}{\partial g_{n+1}}\,Dg_{n+1}[\Delta\theta_{\mathrm{r}}]\right)\boldsymbol{P}^{\alpha}\\ Dg_{n+1}[\Delta\theta_{\mathrm{r}}] &= \mathfrak{K}_1\sum_{\alpha=1}^{N_{\mathrm{s}}}\mathfrak{K}_2^{\alpha}D\tau_{n+1}^{\alpha}[\Delta\theta_{\mathrm{r}}]\end{aligned} \tag{48}$$

and an analogous tensor equation to Equation (45) results,

$$D\mathscr{M}[\Delta\theta_{\mathrm{r}}] : \mathfrak{A} = -\mathfrak{F}\Delta\theta_{\mathrm{r}} \tag{49}$$

where

$$\mathfrak{F} = \frac{1}{3\theta_{\mathrm{r}}}\sum_{\alpha=1}^{N_{\mathrm{s}}}\frac{\partial\dot{\gamma}_{n+1}^{\alpha}}{\partial\tau_{n+1}^{\alpha}}({}^{\mathrm{e}}\boldsymbol{C}_{n+1} : \mathscr{G}^{\alpha})\boldsymbol{P}^{\alpha} + \frac{1}{3\theta_{\mathrm{r}}}\mathfrak{K}_1\left(\sum_{\alpha=1}^{N_{\mathrm{s}}}\mathfrak{K}_2^{\alpha}[{}^{\mathrm{e}}\boldsymbol{C}_{n+1} : \mathscr{G}^{\alpha}]\right)\left(\sum_{\beta=1}^{N_{\mathrm{s}}}\frac{\partial\dot{\gamma}_{n+1}^{\beta}}{\partial g_{n+1}}\,\boldsymbol{P}^{\beta}\right) \tag{50}$$

Please note that, only right-hand sides of the tensor equations, Equations (45) and (49), differ from each other, and the operator $\mathfrak{A}$ remains the same; therefore, the inverse of the operator $\mathfrak{A}$ has to be performed only once to get both linearized terms.

4.3. Adaptive time stepping procedure

The present finite element method together with integration scheme is fully implicit, and hence, the time step is mainly limited by considerations of convergence in the solution of the non-linear equations and accuracy. A simple time stepping procedure based on subdivision of user defined loading history has been implemented in the present work. The user prescribes the loading/displacement boundary condition history and sets the initial time intervals, denoted $\Delta t^{v+1} = t^{v+1} - t^{v}$. An equilibrium solution for the user defined time interval Δt^{v+1} is found within a set of non-uniform sub-increments of size $\Delta t_{\psi_k^{v+1}}\psi_k^{v+1}$ such that

$$\Delta t^{v+1} \equiv \sum_{k=1}^{S^{v+1}}\Delta t_{\psi_k^{v+1}}\psi_k^{v+1} \tag{51}$$

where S^{v+1} denotes a total number of sub-increments each containing ψ_k^{v+1} uniform time sub-steps $\Delta t_{\psi_k^{v+1}}$. The number of sub-increments and sub-steps in each interval is governed by the convergence or divergence of the global finite element and integration algorithms. Initially, the user defined time interval Δt^1 is treated as a single sub-increment with a single sub-step, thus, $S^1 = 1$, $\psi_1^1 = 1$, and $\Delta t_{\psi_1^1} = \Delta t^1$, initially. If convergence is achieved for this interval, the

same Δt is taken for the next interval, and so on. If convergence is not achieved, then the number of sub-steps is increased by one and the size of time step is reduced. This process of adding a sub-step and reducing the time step is repeated until convergence is obtained. Then the algorithm proceeds to the next sub-step. If, at some point partially through the interval, say after p sub-steps out of a total of q sub-steps for the interval, convergence is not achieved, then those p sub-steps already completed, for which convergence has been achieved, are defined as a sub-increment, and the remaining portion ($q - p$ sub-steps) is defined as another sub-increment, and the number of sub-steps in this remaining sub-increment are increased by one ($q - p + 1$) reducing the time step in this remaining portion. This procedure is continued until the interval is completed. The next interval is then initially assumed to have a single sub-increment and the initial time step is defined based on the time step at the end of the previous time interval. If, on the other hand, convergence is achieved for several sub-steps in a row, then those sub-steps are defined as a sub-increment, and the number of sub-steps for the sub-increment on the remaining interval is reduced by one increasing the time step to speed up the computation. This automatic time stepping procedure is robust and finds quickly the optimal time steps.

5. EXAMPLES

As an illustration and verification of the proposed model, we analysed plane strain compression and plane strain simple shear deformations on a unit cell consisting of 51 randomly oriented grains. The overall effective stress–strain curve and texture evolution are compared with results from the Taylor model. It should be noted, however, that such comparison is informative only, because the finite element analysis presented enforces specific strictly homogeneous boundary conditions on the heterogeneous media resulting in non-homogeneous deformation along the edges with homogeneous stresses. A larger sample of grains, and considering only the interior grains, or better yet, proper scale linking through enforcing appropriate boundary conditions, would be required for a more appropriate comparison. In this paper, the main goal is demonstration of the integration and finite element algorithm. Future work includes proper computational homogenization. The geometry of the selected RVE was motivated by a micrograph of an aluminium alloy [35]. This image, with highlighted grain boundaries, is shown in Figure 2(a). Figure 2(b) displays the finite element discretization of the selected unit cell. Note, that grains on boundaries of the unit cell were modified to allow for periodic boundary conditions, which will be considered in future work, as will be mentioned in the Conclusions section. A mixed mesh, primarily consisting of quadrilateral elements, was generated using the $T3D$ generator developed by Rypl [36]. A total of 1746 nodes, 107 P1/P0 triangles and 1617 Q1/Q0 quadrilaterals were used in the discretization of the 0.1×0.1 mm domain. Because of the relatively small number of triangles and the Hu-Washizu finite element formulation, mesh locking does not occur.

The material behaviour is as described in Equations (8)–(13). The properties are selected for Al-1100 at a temperature of 300 K and are listed in Table I. The elastic anisotropy of aluminium, which is small, is neglected in this analysis, and the elastic Lamè parameters are taken to be $\mu_e = 25.30$ GPa and $\lambda_e = 54.41$ GPa. Aluminium is face-centred-cubic and the usual primary twelve $\{111\}\langle\bar{1}10\rangle$ slip systems are considered. The $\langle 111\rangle$ pole figures depicting the initial random texture of the unit cell are shown in Figure 3.

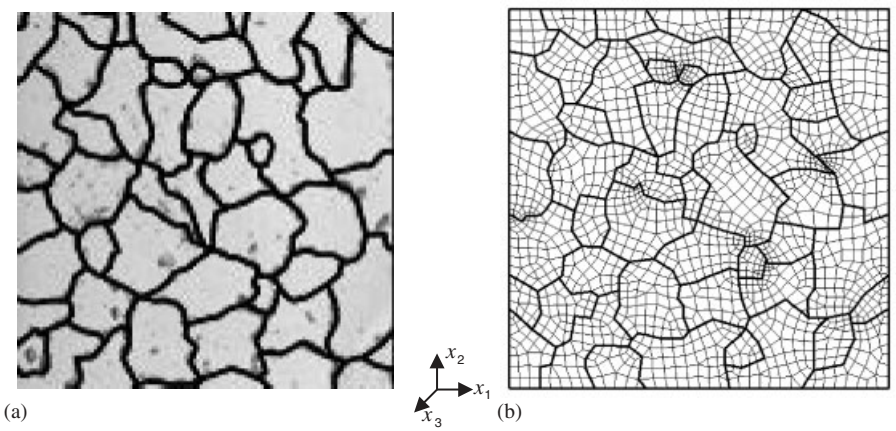

Figure 2. (a) Micrograph; and (b) FE representation of the unit cell.

Table I. Viscoplastic properties of Al-1100.

m	g_0	$\dot{\gamma}_0$	G_0	g_{s_0}	$\dot{\gamma}_s$	ω
0.005	27.17 MPa	$1.0\,s^{-1}$	58.41 MPa	61.80 MPa	$5.0 \times 10^{10}\,s^{-1}$	5.0988×10^{-6}

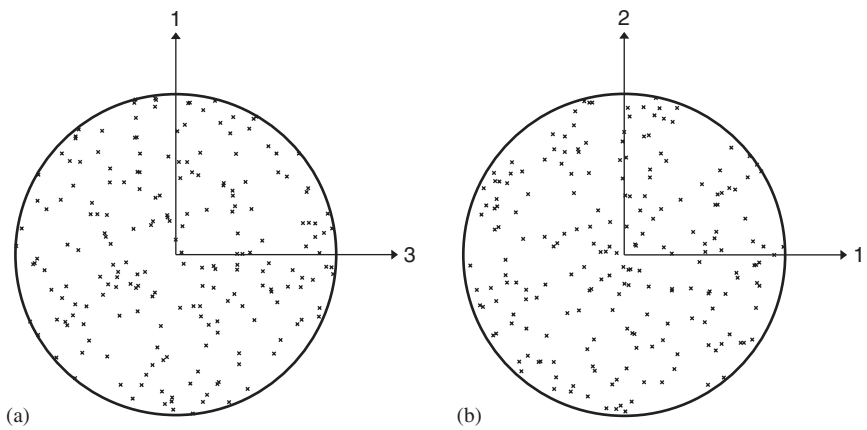

Figure 3. The $\langle 111 \rangle$ pole figures of initial 51 grain orientations.

The deformations considered, as mentioned above, are plane strain compression and simple shear. For the case of plane strain compression, the displacement $\breve{u}$ is applied in the $-x_2$ direction to the top of the unit cell, and in the case of simple shear, the displacement $\breve{u}$ is applied in the $+x_1$ direction to the top of the unit cell. In both cases, the bottom of the unit cell is fixed in the x_2 direction. For plane strain compression, only the lower left-hand

corner is fixed in the x_1 direction to prevent rigid body motion, whereas for simple shear, the whole length of the bottom edge is fixed in the x_1 direction. The time over which the total deformation occurs is denoted t_{tot}. The macroscopic deformation gradients associated with these deformations, assuming incompressible behaviour, are for plane strain compression

$$\underline{\boldsymbol{F}}_{n+1} = \begin{bmatrix} \dfrac{t_{\text{tot}}}{t_{\text{tot}} + t_{n+1}\breve{\varepsilon}} & 0 & 0 \\ 0 & 1 + \dfrac{t_{n+1}}{t_{\text{tot}}}\breve{\varepsilon} & 0 \\ 0 & 0 & 1 \end{bmatrix}$$

and for simple shear

$$\underline{\boldsymbol{F}}_{n+1} = \begin{bmatrix} 1 & \dfrac{t_{n+1}}{t_{\text{tot}}}\breve{\varepsilon} & 0 \\ 0 & 1 & 0 \\ 0 & 0 & 1 \end{bmatrix}$$

where $\breve{\varepsilon} = \breve{u}/l$ and l is the length of a side of the unit cell. In the comparative analyses where the Taylor model was used, these deformation gradients were applied to each grain. Those simulations were carried out using the integration algorithm described in Section 3 and the same results were obtained using the integration algorithm presented in Reference [23].

The resulting local and macroscopic behaviour are characterized by the effective plastic strain and von Mises effective stress. The local effective plastic strain ${}^{\text{p}}\varepsilon_{\text{eff}}$ and effective stress σ_{eff} are computed as,

$${}^{\text{p}}\varepsilon_{\text{eff}} = \int_0^t \sqrt{\tfrac{2}{3}\,{}^{\text{p}}\hat{\boldsymbol{D}} \cdot {}^{\text{p}}\hat{\boldsymbol{D}}}\,\mathrm{d}t'$$

and

$$\sigma_{\text{eff}} = \sqrt{\tfrac{3}{2}\boldsymbol{\sigma}' \cdot \boldsymbol{\sigma}'}$$

where

$${}^{\text{p}}\hat{\boldsymbol{D}} \equiv \text{sym}({}^{\text{p}}\hat{\boldsymbol{L}})$$

The macroscopic response of the unit cell is described by the average rate of deformation and stress tensors, denoted by underline (_), which are computed as a volume averages of the local fields,

$${}^{\text{p}}\underline{\hat{\boldsymbol{D}}} = \frac{1}{v}\int_v {}^{\text{p}}\hat{\boldsymbol{D}}\,\mathrm{d}v, \quad \underline{\boldsymbol{\sigma}} = \frac{1}{v}\int_v \boldsymbol{\sigma}\,\mathrm{d}v$$

where v is the volume of the deformed unit cell. The macroscopic effective plastic strain and stress are then computed analogously to the local fields as

$${}^{\text{p}}\underline{\varepsilon_{\text{eff}}} = \int_0^t \sqrt{\tfrac{2}{3}\,{}^{\text{p}}\underline{\hat{\boldsymbol{D}}} \cdot {}^{\text{p}}\underline{\hat{\boldsymbol{D}}}}\,\mathrm{d}t'$$

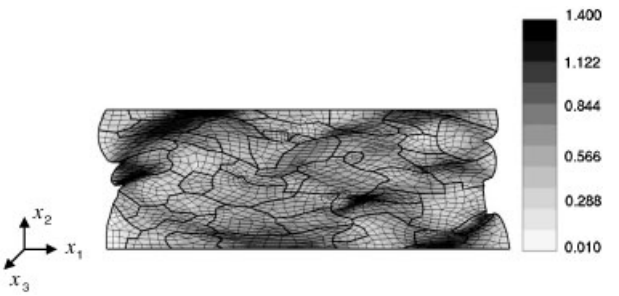

Figure 4. The effective plastic strain ${}^{\mathrm{p}}\varepsilon_{\mathrm{eff}}$ after 40% plane strain compression of the unit cell.

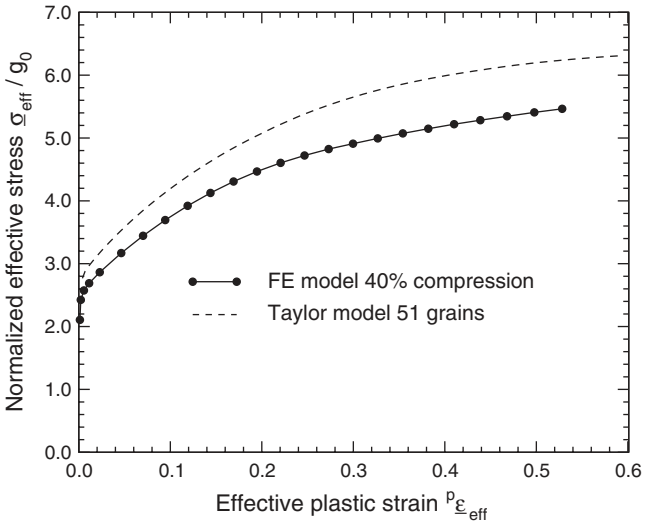

Figure 5. The overall effective stress–strain behaviour for plane strain compression.

and

$$\underline{\sigma_{\mathrm{eff}}} = \sqrt{\tfrac{3}{2}\underline{\boldsymbol{\sigma}}' \cdot \underline{\boldsymbol{\sigma}}'}$$

First, consider the plane strain compression case. The unit cell is compressed by 40% ($\breve{\varepsilon} = -0.4, \breve{u} = -0.04\,\mathrm{mm}$) along the x_2 axis over a time of $t_{\mathrm{tot}} = 40\,\mathrm{s}$ with $\dot{\breve{u}} = -0.001\,\mathrm{mm/s}$ constant. The average time step needed for convergence was found to be $\Delta t = 0.14\,\mathrm{s}$. Figure 4 shows deformation of the unit cell and the meso-scale effective plastic strain, and Figure 5 shows the effective stress–strain response along with that predicted using the Taylor model. As can be seen from Figure 4, the deformation on the lateral boundaries is strongly non-homogeneous, leading to greater localization, and thus, softer response, than would be expected from either a Taylor model, as seen in Figure 5, or a multi-scale model with appropriate boundary conditions. The predicted textures for both the Taylor and finite element models at the final compression of 40% are displayed in Figure 6. As expected, a stronger texture was obtained from the Taylor

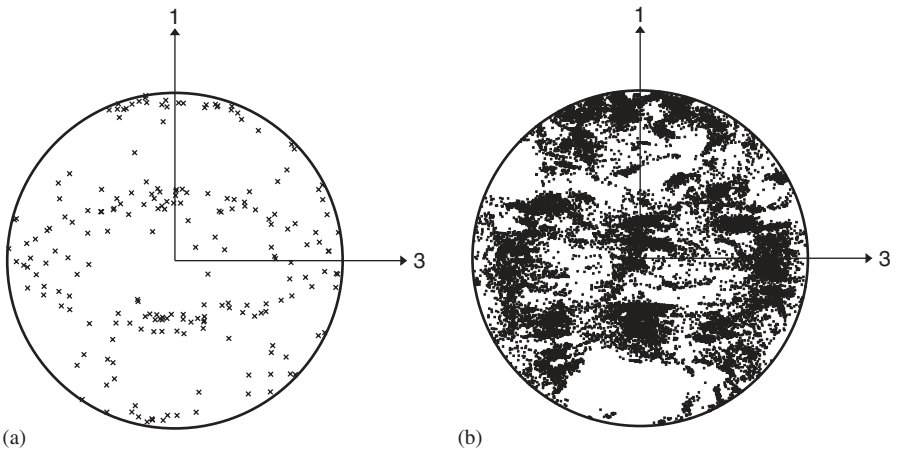

Figure 6. The ⟨111⟩ pole figures after 40% plane strain compression of the unit cell: (a) Taylor model; and (b) finite element model.

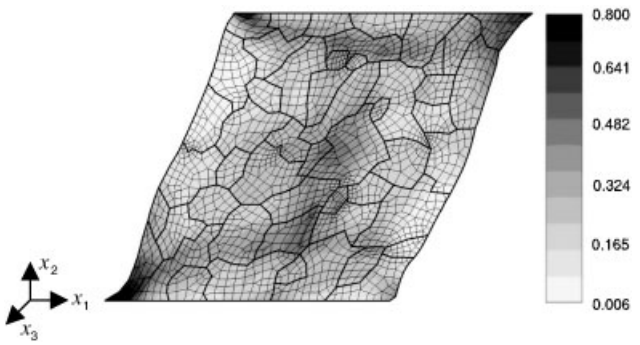

Figure 7. The effective plastic strain ${}^{\mathrm{p}}\varepsilon_{\mathrm{eff}}$ after 50% plane strain simple shear of the unit cell.

model, which over-predicts the final texture. It should be noted also that more poles are plotted from the finite element model after compression because the grains deform non-homogeneously resulting in different parts of a single grain having different orientations, although that grain had a single orientation at the start. An orientation pole is plotted for each integration point in the finite element discretization.

In the next example, we compare the stress–strain response and texture prediction obtained with both the Taylor and finite element models for plane strain simple shear. The unit cell is sheared by $\breve{\varepsilon} = 0.5, \breve{u} = 0.05\,\mathrm{mm}$ over a time of $t_{\mathrm{tot}} = 50\,\mathrm{s}$ with $\dot{\breve{u}} = 0.001\,\mathrm{mm/s}$ constant. The average time step needed for convergence was found to be $\Delta t = 0.2\,\mathrm{s}$ in this example. As one may expect, the strain localization is more dominant for this type of loading as shown in Figure 7. The reaction shear forces are localized to the top right and bottom left corners, where the effective plastic strain is more developed. Such localized behaviour influences substantially the macroscopic stress–strain response of the RVE, as shown in Figure 8. Figure 9 shows

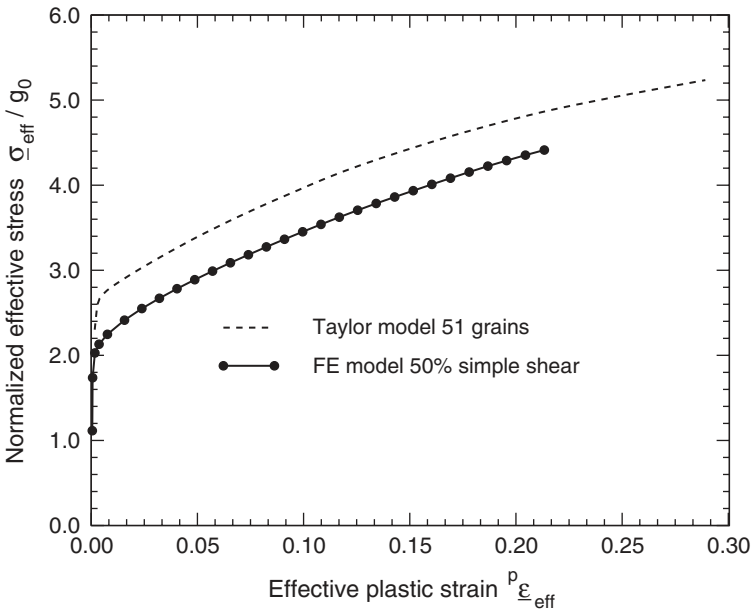

Figure 8. The overall effective stress–strain behaviour for plane strain simple shear.

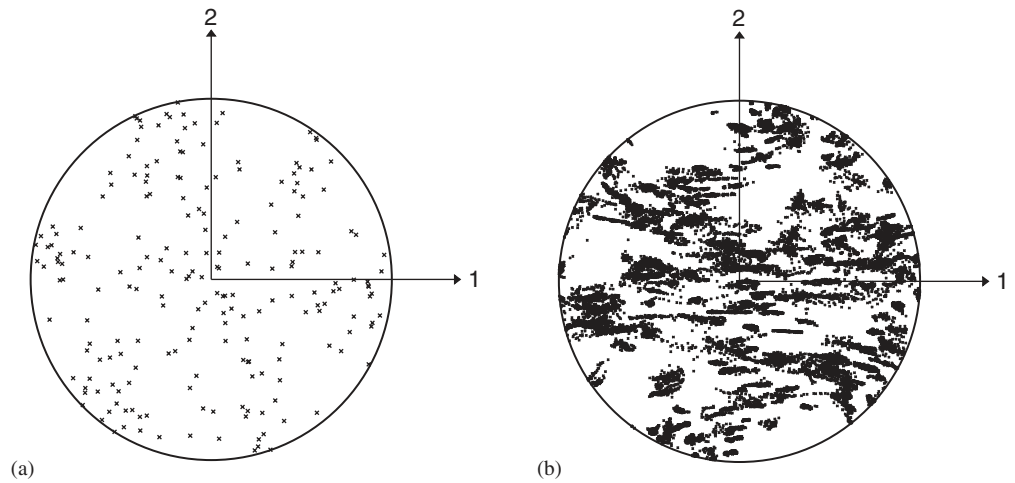

Figure 9. The ⟨111⟩ pole figure after 50% plane strain simple shear of the unit cell: (a) Taylor model; and (b) finite element model.

comparison of ⟨111⟩ pole figures for both the Taylor and finite element models. The texture is not strongly developed in this case due to the continual rotation of the principle directions during the deformation. The main observation worth noting again is the spreading of the orientations in the finite element model due to the non-homogeneous deformations in the grains.

6. CONCLUSIONS

The proposed computational model is shown to be effective in modelling elasto-viscoplastic behaviour and texture evolution in a polycrystal subject to finite strains. The finite element framework, based on an updated Lagrangian formulation, adopts a kinematic split of the deformation gradient into volume preserving and volumetric parts together with a three-field form of the Hu-Washizu variational principle to create a stable finite element method. The consistent linearization of the resulting system of nonlinear equations is derived.

The meso-scale is characterized by a representative volume element and is capable of predicting local non-homogeneous stress and deformation fields. The numerical analysis of plane strain compression and simple shear loading of a unit cell was compared to the widely used Taylor model. Such comparison is for information only, because the finite element analysis is influenced by the specific homogeneous boundary conditions resulting in non-homogeneous deformation on lateral boundaries.

The present work is a first step toward linking the macro-scale to the meso-scale through computational homogenization, where a meso-structure is fully coupled with the deformation at a typical material point of a macro-continuum. In this work, the appropriate periodic boundary conditions have not yet been derived. Further, on-going work involves extending the present model to cover macro–meso transition including periodic fields.

ACKNOWLEDGEMENTS

This material is based upon work supported by the National Science Foundation under Grant Nos. (CMS-0084987, DMI-0115330, DMI-0115146) and by Alcoa, Inc.

REFERENCES

1. Taylor GI, Elam CF. The plastic extension and fracture of aluminum crystals. *Proceedings of the Royal Society of London* 1925; **A108**:28–51.
2. Hill R, Rice JR. Constitutive analysis of elasto-plastic crystals at arbitrary strain. *Journal of the Mechanics and Physics of Solids* 1972; **20**:401–413.
3. Peirce D, Asaro RJ, Needleman A. Material rate dependence and localized deformation in crystalline solids. *Acta Metallurgica* 1983; **31**(12):1951–1976.
4. Taylor GI. Plastic strain in metals. *Journal of the Institute of Metals* 1938; **62**:307–324.
5. Asaro RJ, Needleman A. Texture development and strain hardening in rate dependent polycrystals. *Acta Metallurgica* 1985; **33**(6):923–953.
6. Chastel YB, Dawson PR. Equilibrium-based model for anisotropic deformations of polycrystalline materials. *Materials Science Forum* 1994; **156–157**(2):1747–1752.
7. Molinari A, Canova GR, Azhi A. A self-consistent approach of the large deformation polycrystal viscoplasticity. *Acta Metallurgica* 1987; **35**(12):2983–2994.
8. Harren SV, Asaro RJ. Nonuniform deformations in polycrystals and aspects of the validity of the Taylor model. *Journal of the Mechanics and Physics of Solids* 1989; **37**:191–232.
9. Bronkhorst CA, Kalidindi SR, Anand L. Polycrystalline plasticity and the evolution of crystallographic texture in fcc metals. *Philosophical Transactions of the Royal Society of London* 1992; **A341**:443–477.
10. Becker R, Panchanadeeswaran S. Effects of grain interactions on deformation and local texture in polycrystals. *Acta Metallurgica et Materialia* 1995; **43**:2701–2719.
11. Beaudoin AJ, Mecking H, Kocks UF. Development of localized orientation gradients in fcc polycrystals. *Philosophical Magazine A* 1996; **73**:1503–1518.
12. Busso EP, Meissonnier FT, O'Dowd NP. Gradient-dependent deformation of two-phase single crystals. *Journal of the Mechanics and Physics of Solids* 1999; **48**:2333–2361.

13. Beaudoin AJ, Acharya A, Chen SR, Korzekwa DA, Stout MG. Consideration of grain-size effect and kinetics in the plastic deformation of metal polycrystals. *Acta Materialia* 2000; **48**:3409–3423.
14. Sarma GB, Radhakrishnan B, Dawson PR. Mesoscale modeling of microstructure and texture evolution during deformation processing of metals. *Advances in Engineering Materials* 2002; **4**:509–514.
15. Marin EB, Dawson PR. Elastoplastic finite element analyses of metal deformations using polycrystal constitutive models. *Computer Methods in Applied Mechanics and Engineering* 1998; **165**:23–41.
16. Brezzi F, Fortin M. *Mixed and Hybrid Finite Element Methods*. Springer: New York, 1991.
17. Simo JC, Taylor RL, Pister KS. Variational and projection methods for the volume constraint in finite deformation elasto-plasticity. *Computer Methods in Applied Mechanics and Engineering* 1985; **51**:177–208.
18. Hughes TJR. Generalization of selective integration procedures to anisotropic and nonlinear materials. *International Journal for Numerical Methods in Engineering* 1980; **15**:1413–1418.
19. Moran B, Ortiz M, Shih CF. Formulation of implicit finite element methods for multiplicative finite deformation plasticity. *International Journal for Numerical Methods in Engineering* 1990; **29**:483–514.
20. Klaas O, Maniatty AM, Shephard MS. A stabilized mixed finite element method for finite elasticity. Formulation for linear displacement and pressure interpolation. *Computer Methods in Applied Mechanics and Engineering* 1999; **180**:65–79.
21. Lee EH. Elastic-plastic deformation at finitestrains. *Journal of Applied Mechanics* 1969; **36**:1–6.
22. Hill R. Generalized constitutive relation for incremental deformation of metals crystals by multisplit. *Journal of the Mechanics and Physics of Solids* 1966; **14**:95–102.
23. Maniatty AM, Dawson PR, Lee YS. A time integration algorithm for elasto-plastic cubic crystals applied to modelling polycrystalline deformation. *International Journal for Numerical Methods in Engineering* 1992; **35**:1565–1588.
24. Mathur KK, Dawson PR. On modeling the development of crystallographic texture in bulk forming processes. *International Journal of Plasticity* 1989; **5**:67–94.
25. Voce E. A practical strain-hardening function. *Acta Metallurgica* 1948; **51**:219–226.
26. Kocks UF. Laws for work-hardening and low-temperature creep. *Journal of Engineering Materials and Technology* 1976; **98**:76–85.
27. Miller M, Dawson P. Influence of slip system hardening assumptions on modeling stress dependence of work hardening. *Journal of the Mechanics and Physics of Solids* 1997; **45**(11/12):1781–1804.
28. Miehe C. Exponential map algorithm for stress updates in anisotropic multiplicative elastoplasticity for single crystals. *International Journal for Numerical Methods in Engineering* 1996; **39**:3367–3390.
29. Ortiz M, Stainier L. The variational formulation of viscoplastic constitutive updates. *Computer Methods in Applied Mechanics and Engineering* 1999; **171**:419–444.
30. Simo JC, Taylor RL. Consistent tangent operators for rate-independent elastoplasticity. *Computer Methods in Applied Mechanics and Engineering* 1985; **48**:101–118.
31. Nagtegaal JC, Parks DM, Rice JR. On numerical accurate finite element solutions in the fully plastic range. *Computer Methods in Applied Mechanics and Engineering* 1974; **4**:153–177.
32. Davis TA, Duff IS. An unsymmetric-pattern multifrontal method for sparse LU factorization. *SIAM Journal of Matrix Analysis and Applications* 1997; **18**(1):140–158.
33. Davis TA, Duff IS. A combined unifrontal/multifrontal method for unsymmetric sparse matrices. *ACM Transactions of Mathematical Software* 1999; **25**(1):1–19.
34. UMFPACK page. http://www.cise.ufl.edu/research/sparse/umfpack/
35. Misiolek WZ. Private communication, 2002.
36. Rypl D, Bittnar Z. Hybrid method for generation of quadrilateral meshes. *Engineering Mechanics* 2002; **9**(1/2):49–64.

